Laser-excited shear waves in solid and liquid two-dimensional dusty plasmas

A. Piel[a)]
IEAP, Christian-Albrechts-Universität, D-24098 Kiel, Germany

V. Nosenko and J. Goree
Department of Physics and Astronomy, The University of Iowa, Iowa City, Iowa

(Received 30 January 2006; accepted 24 March 2006; published online 27 April 2006)

The propagation of transverse waves in a two-dimensional particle suspension in a plasma is studied in the solid and liquid phase. The different states of the suspension are realized by raising the kinetic temperature of the dust particles with a new laser method. An additional laser beam is used to excite shear waves and the wave is observed by videomicroscopy in terms of the individual velocities of the dust particles. For recovering the spatial wave patterns the method of singular value decomposition is applied and compared with the method of spatial Fourier analysis of complex wave numbers. In the solid phase, weakly damped waves are found which follow the expected dispersion relation. In the liquid phase the existence of strongly damped waves is demonstrated. The real part of the wave number is in overall agreement with the predictions of the Quasi Localized Charge Approximation model for a two-dimensional system. The damping of the waves is discussed. © *2006 American Institute of Physics*. [DOI: 10.1063/1.2196327]

I. INTRODUCTION

Waves in dusty plasmas reveal many inherent features of the interactions in strongly coupled Coulomb systems.[1] There was a particular interest in the wave phenomena in two-dimensional (single layer) suspensions of dust particles in a plasma, which exhibit compressional and shear modes,[2–6] Mach cones[7–9] or dipole radiation from localized sources,[10] which are now well understood. The situation for the liquid phase is quite different. An ordinary liquid supports compressional (sound) waves but transverse shear modes can only propagate in the limit of wavelengths as short as a few molecular spacings. Strongly coupled dusty plasmas in the liquid phase can support shear waves, as was shown by Kaw and Sen[11,12] in terms of a viscoelastic model, which predicted propagating waves with acoustic dispersion at high frequency and become purely damped at low frequencies. Recent calculations with the quasilocalized charge approximation (QLCA) (Ref. 13) show that the shear mode is also acoustic at low frequencies. Shear waves in the liquid phase were also studied in molecular dynamics (MD) simulations,[14] which show that the waves have a long-wavelength cutoff that is also found in analytical models.[15] A critical comparison between the QLCA model and MD simulations was recently made by Kalman *et al.*[16]

On the experimental side, wave phenomena in the liquid states of the plasma suspension with particle motion in the horizontal plane were studied by Nunomura *et al.*[17] In these experiments the thermally excited spectra of longitudinal and transverse phonons were studied in the solid and liquid phase of the plasma suspension. The temperature was varied by increasing the number of perturbing particles in a lower layer. The color graphs (in the online version of the article) show that in the solid phase the shear wave dispersion is acoustic starting at $k=0$, $\omega=0$. In the liquid phase the high frequency part is reduced in intensity. No long wavelength cutoff was reported. Instead, the frequency spectrum of the long-wavelength modes is extremely broadened. The transverse wave that was observed in Ref. 17, and which we study in the present article, are for particle motion in the horizontal plane where all the particles are suspended. A different kind of transverse wave in a liquid phase was reported by Pramanik *et al.*[18] These waves incorporate a vertical motion of the particles, where the restoring force is provided by gravity and the electric field that levitates the particles.

The present article describes new shear wave experiments for a single layer particle suspension in the solid phase, at the melting point, and in the liquid phase. Different from the study in Ref. 17, the waves are excited with a periodic laser force. For the recovery of the wave signals from the particle velocities the method of singular value decomposition (SVD) is used and compared with the spatial Fourier analysis of complex wave numbers.

The outline of the paper is as follows: In Sec. II we describe the experimental setup and laser heating method. Section III summarizes the spatial Fourier analysis of complex wave numbers. Section IV introduces the SVD method in terms of test data. The dispersion of externally excited shear waves is studied in Sec. V for the solid phase and in Sec. VI for the liquid state. The damping of the waves is discussed in Sec. VII. Section VIII gives a summary and conclusions.

II. EXPERIMENTAL SETUP AND PROCEDURE

The experiments were performed in the modified GEC reference cell at The University of Iowa.[8] A single-layer suspension consisting of spherical melamine-formaldehyde

[a)]Electronic mail: piel@physik.uni-kiel.de

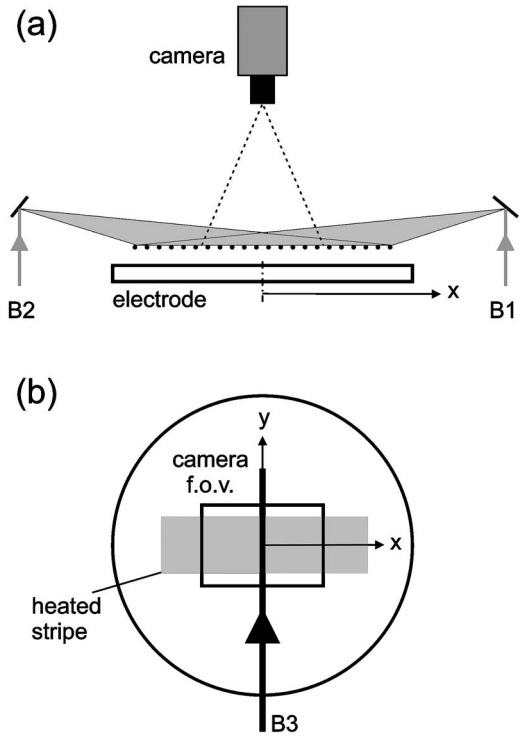

FIG. 1. (a) Side view of the single-layer particle suspension. Two laser beams (B1, B2) are used for heating by exerting a quasirandom force. The waves are observed with a CCD camera. (b) Top view. The waves are excited with a sinusoidally modulated Ar^+ laser beam (B3). The shear waves propagate in the $\pm x$ directions. The camera field of view and the heated stripe are marked. The excitation region for shear waves is shown as the thick black line along the y axis.

(MF) particles with (8.09 ± 0.18) μm diameter is formed in the sheath of a radio frequency plasma. The discharge is operated at 13.56 MHz in room-temperature argon at 5 mTorr. Figure 1(a) shows a side view of the particle suspension, which is levitated above the rf powered electrode, together with two laser beams (B1 and B2) used for heating the plasma crystal. The symmetrical laser beam arrangement ensures that the heating laser exerts no net force on the suspension. The footprint of the laser beams are deflected in the x and y directions using a pair of galvanometer mirrors to form an elongated Lissajous figure with deflection frequencies $f_x=9.0$ Hz and $f_y=14.5623$ Hz. More details of this heating technique are described in a companion paper.[19] The heating beams at 532 nm wavelength have equal power and the heated stripe in the suspension is represented by the shaded part in the camera's field of view [Fig. 1(b)].

The shear waves are excited by a third laser beam (B3) of an argon ion laser, which illuminates a narrow excitation region that is aligned with the y direction and exerts a periodic force in the y direction, as shown in Fig. 1(b). The power of beam B3 is sinusoidally modulated by means of a galvanometer mirror, which gradually blocks part of the beam. This resulted in shear waves that propagated in $\pm x$ directions, traveling away from the excitation region. The quality of the sine wave was ensured by monitoring the harmonics of the laser power, which together were −25 dB below the fundamental. The modulation degree is 100%. The excitation laser power (measured inside the plasma chamber) is chosen as 0.23 W for the solid phase to minimize bond breaking, and 0.46 W for the liquid phase for increased wave amplitude in order to improve the signal to noise ratio of the wave.

Because our particle suspension has a finite diameter, the shear waves excited by this excitation laser do not have infinite wavefronts, so that they require a return oscillatory circulatory flow at large distances. This circulatory shear flow would ideally take place outside the field of the camera so that we could model the waves as having the properties of infinite wavefronts in an unbounded suspension. During the course of the experiment, it appeared that this was achieved, although there was actually a finite shear flow in the field of view which we detected in subsequent analysis of the velocity data. This shear flow must be taken into account when considering some of our data, as we explain later.

The camera field of view is 22.7 mm wide (x) by 17.0 mm high (y) at a resolution of 640×480 pixel. The camera is operated at a frame rate of 30 fps. Each experiment is comprised of 2400 frames. The particle positions are measured with subpixel resolution. The velocity of each particle is obtained from the particle displacement in subsequent frames.

The experiments presented here consist of two series. The first series concerns wave excitation in the solid phase of the particle suspension. The shear waves are studied for excitation frequencies of 1 Hz, 2 Hz, …, 6 Hz. The suspension of particles rotated clockwise at an angular velocity of $\omega_{\mathrm{rot}}\approx1\ \mathrm{min}^{-1}$, which corresponds to a much lower frequency than any of the waves that we observe. In our data analysis, we will filter out this rotational motion, as discussed later.

From the mean-square velocities of the particle motion in the x and y direction the temperatures T_x and T_y are computed as a function of the y position. Figure 2(a) shows that the temperature profile is fairly homogeneous in the central part $3.6\ \mathrm{mm}<y<12.0$ mm. Therefore the region between the dashed lines is used for evaluating the shear waves. On the other hand, we find that $T_x>T_y$. This anisotropy can be attributed to the application of the laser forces in the x direction and the subsequent collisional scattering of the particle momentum into the perpendicular y direction. The particle motion is continuously cooled by dust-neutral friction, which results in the lower value of T_y.

The dust temperature increases with the applied heating laser power [Fig. 2(b)]. This graph is used to interpolate the dust temperature at the heating laser power of 1.9 W. From the dust temperatures the coupling coefficients $\Gamma_{x,y}=(Z_de)^2/(4\pi\epsilon_0 akT_{x,y})$ are calculated. The coupling coefficient is the ratio of the potential energy of a dust particle to its typical kinetic energy. Matter is said to be strongly coupled when $\Gamma>1$. For the unit length a we use the Wigner-Seitz radius defined as in Ref. 16. We computed its value from the lattice constant $b=615$ μm of the crystal, which we measured for zero laser heating power as the radius of the first peak of the pair correlation function. This was done using the relationship $a=3^{1/4}(2\pi)^{-1/2}b$ for a perfect triangular 2D lattice. We use the Wigner-Seitz radius in defining the coupling coefficient $\Gamma_{x,y}$, the shielding factor $\kappa=a/\lambda_D$, and the 2D dust plasma frequency $\omega_{\mathrm{pd}}^{(2D)}$, where the

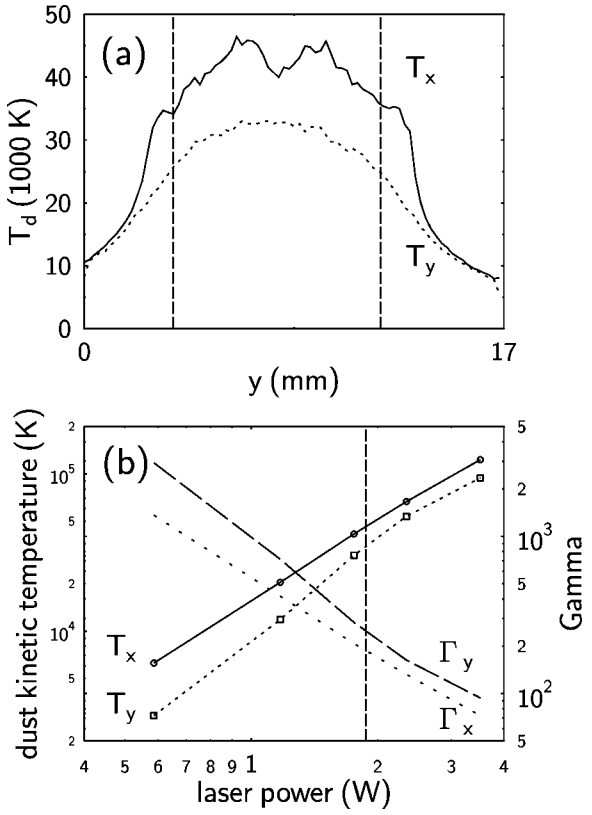

FIG. 2. (a) Dust temperature profiles $T_x(y)$ and $T_y(y)$ across the laser heated stripe at 1.9 W heating power. The central part between 3.6 mm and 12 mm is homogeneous within ±10%. (b) Increase of the dust temperatures with laser power. The dust temperature T_x is larger than T_y. The graph also includes the resulting values of $\Gamma_{x,y}$. Note that at 1.9 W the system is close to melting ($\Gamma \approx 200$).

latter is defined as in Ref. 16. We note that some authors define the coupling coefficient differently, using the mean interparticle distance as the unit length.[11,12] Using values of the dust charge number $Z_d = -12\,800$ and the screening length λ, both computed from measurements of the propagation velocity of compressional and shear wave pulses,[9] we find $\kappa = 0.43$, $\omega_{pd}^{(2D)} = 72.6\ \mathrm{s}^{-1}$, and the values of the coupling constant reported in Fig. 2.

III. SPATIAL FOURIER ANALYSIS OF COMPLEX WAVE NUMBERS

The method used earlier[5] for recovering amplitude and phase of an externally excited sinusoidal wave from the velocity fluctuations $v_y(x,t)$ begins with projecting the time series on a sine and cosine function at the well defined exciter frequency ω_{ex}. For a shear wave that propagates in the x direction this is done by estimating the discrete Fourier transform as $v_y(x) \approx \sum_{k=1}^{N} v_y(x,t)[\cos(\omega_{\mathrm{ex}} t_k) + i \sin(\omega_{\mathrm{ex}} t_k)]$, N being the number of samples.[20] In this way the amplitude $|v_y(x)|$ and phase $\varphi(x) = \arctan\{\mathrm{Im}[v_y(x)]/\mathrm{Re}[v_y(x)]\}$ of the wave are recovered as a function of position. The spatial evolution of the phase gives the real part $k_r = \mathrm{d}\varphi(x)/\mathrm{d}x$ of the wave number and the logarithmic decay of the amplitude gives the imaginary part $k_i = \mathrm{d}\ln(|v_y(x)|)/\mathrm{d}x$. An example for this technique is given below in Fig. 6. In the following, we will refer to this method as spatial Fourier analysis of complex wave numbers (SFACW). We will use both the SFACW and the SVD analysis described in the next section to measure k_r and k_i; by repeating these measurements as a function of the exciter frequency we will produce the dispersion relation.

IV. SVD ANALYSIS

Singular value decomposition (SVD) (also known as biorthogonal decomposition) is a suitable tool to extract wave phenomena in plasmas from spatiotemporal data.[21,22] The method was mostly used by the plasma fusion community (see examples in Ref. 22 and more recently Refs. 23 and 24). It was also used to detect irregularities in the solar cycle.[25] Very recently, it was applied in dusty plasmas to detect the driving modes in the melting process of a plasma crystal.[26]

The method uses a set of spatiotemporal data of any fluctuating quantity, for example density, temperature, light emission or particle velocities, $y(x_j, t_i)$ at positions x_j, $j = 1, \ldots, M$, sampled at times $t_i, i = 1, \ldots, N$. This data set is arranged into an $N \times M$ matrix $\boldsymbol{Y}$, in which the columns are the time series $Y_{ij} = y(x_j, t_i)$. It is assumed that $N > M$. The singular value decomposition transforms the matrix $\boldsymbol{Y}$ into the product

$$\boldsymbol{Y} = \boldsymbol{C}\boldsymbol{W}\boldsymbol{T}^{\mathsf{T}}, \tag{1}$$

in which $\boldsymbol{C}$ is an $N \times M$ column-orthogonal matrix, $\boldsymbol{W}$ is an $M \times M$ diagonal matrix, and $\boldsymbol{T}$ is an $M \times M$ orthogonal matrix. The column vectors of $\boldsymbol{C}$ are called *chronos* and the column vectors of $\boldsymbol{T}$ are called *topos*. The diagonal of the matrix $\boldsymbol{W}$ contains positive weight factors in decreasing order. In this way the original spatiotemporal data set can be written as

$$y(x_j, t_i) = \sum_{k=1}^{M} w_k T_k(x_j) C_k(t_i). \tag{2}$$

The physical meaning of this decomposition is that the leading members of this sum give an approximative representation of the original spatiotemporal data. The square of the weight factor w_k^2 is called *signal energy* of the mode k. Different from a Fourier analysis, the SVD eigenfunctions are in general no Fourier modes but pertinent features of the measured signals. When the spatiotemporal signal contains travelling waves the weight spectrum contains pairs of equal weight factors.[21,27] In the special case of a harmonic wave $y(x,t) = y_0 \cos(kx - \omega t)$, the pair of chronos and topos associated with this mode become Fourier modes.

As an example for the recovery of wave signals by the SVD technique and to introduce the typical representation of the SVD analysis we have analyzed the following surrogate signal:

$$y(x,t) = y_1 \cos(k_1 x - \omega_1 t) + y_2 \cos(k_2 x - \omega_2 t) + y_3 \cos(k_3 x - \omega_3 t) + y_4\ \mathrm{gauss}(t), \tag{3}$$

which consists of three waves with different amplitudes $y_1 = 1$, $y_2 = 0.1$, $y_3 = 0.01$ that span two decades and with incommensurate frequencies $\omega_1 = 5$, $\omega_2 = 7$, $\omega_3 = 13$. The wave numbers of these three waves are chosen as $k_1 = 5/3$, $k_2 = 7/3$,

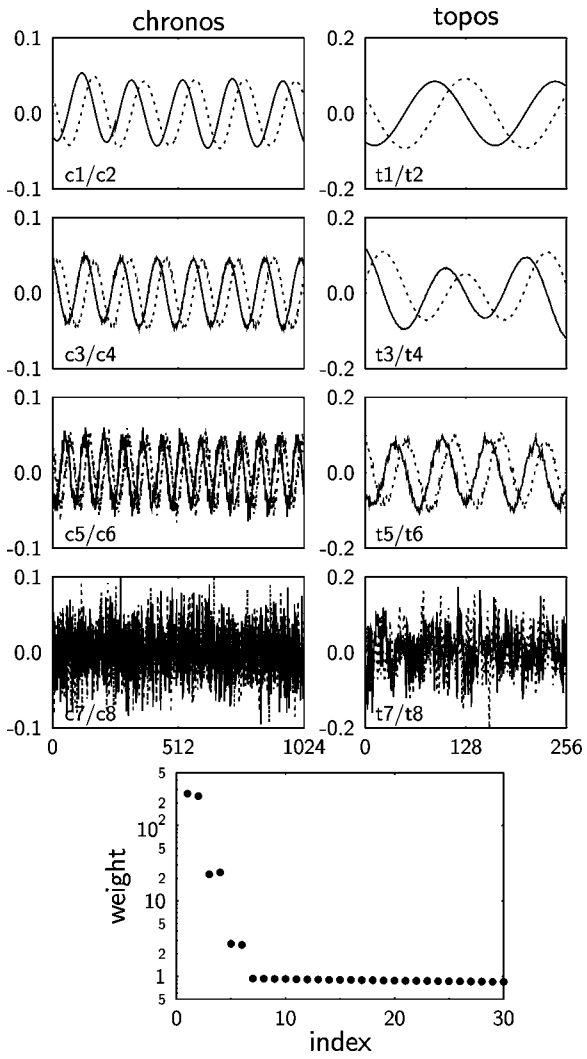

FIG. 3. SVD analysis of surrogate data representing three independent waves embedded in noise. The pairs of weights (bottom panel) are an indicator for propagating waves. The relative amplitudes of the three waves are quantitatively recovered. Chronos and topos 1, 3, 5, 7 are displayed as full lines, modes 2, 4, 6, 8 as dashed lines.

$k_3=13/3$ to mimic acoustic dispersion with a constant phase velocity. The waves are embedded in Gaussian noise with a standard deviation $y_4=2y_3$, which exceeds the amplitude of the weakest wave.

In Fig. 3 the decomposition into chronos and topos and the distribution of weights are compiled. The three waves of the original signal are now represented by the first six SVD modes $(c_1t_1-c_6t_6)$. These modes form pairs of sine and cosine-like functions. A pair of such functions is necessary to describe the proper amplitude and phase of the original wave. The wave with amplitude y_1 is now represented by the pair c_1t_1 and c_2t_2. The SVD modes c_7t_7 and c_8t_8 and higher modes appear as noise. Note that the weakest wave mode, represented by c_5t_5 and c_6t_6, can be clearly recovered although its amplitude is weaker than the standard deviation of the Gaussian noise. In this sense SVD can be used to separate coherent and stochastic aspects of a signal.

In Table I the weight factors of the first ten modes and their percent fraction of total signal energy are compiled. The first two modes represent already 99.1% of the signal energy. The successful recovery of the weakest wave mode from the noise background becomes evident from comparing the weights of modes 5/6 with any of the individual higher modes (7-256). The power fraction of noise in the original signal was 0.04%. Hence these higher modes, which comprise 0.078% of the total signal energy, contain both noise and residues from the orthogonalization of the low order modes.

TABLE I. Weight factors and signal energies of the SVD modes in Fig. 3.

Mode number	Weight factor	Signal energy
1	264.4	53.3%
2	245.3	45.8%
3	22.58	0.38%
4	23.90	0.43%
5	2.710	0.0055%
6	2.614	0.0052%
7	0.938	
8	0.935	
9	0.928	
10	0.919	
11–256		0.078%

We have performed additional tests to simulate the experimental situation with damped shear waves excited by a line source. For negligible damping we find a pair of SVD modes with equal weights, when a pair of waves emanates symmetrically but with opposing phase velocity from the central source region. The situation changes slightly, when the waves are damped. Then the leading two SVD modes show different weights and the ratio of the weights, w_2/w_1, decreases monotonically from 1 to 0.49 when the imaginary part of the wave number k_i is increased from 0% to 80% of the real wave number. The tests show further that this asymmetry has practically no influence on the recovery of the wave number and damping, which were found within $<3\%$ of their exact values.

V. SHEAR WAVES IN THE SOLID PHASE

The excitation laser exerts a periodic shear force to the crystal in the y direction that is localized to a narrow stripe in the center of the field of view. While the particle motion in the wave is in the y direction, the shear waves propagate in the $\pm x$ directions. Because our method of exciting waves is steady in time, the frequency ω is real, whereas the wave number k is complex corresponding to the damping of a wave that propagates away from the spatial region where it is excited.

For recovering the shear wave, the velocities of all particles are determined for 2048 subsequent video frames. Since we are interested in the velocity field $v_y(x,t)$ in each frame, the x axis is divided into 256 bins and the particle velocities are assigned to the bins using linear interpolation according to the cloud-in-cell technique.[28] In this way the

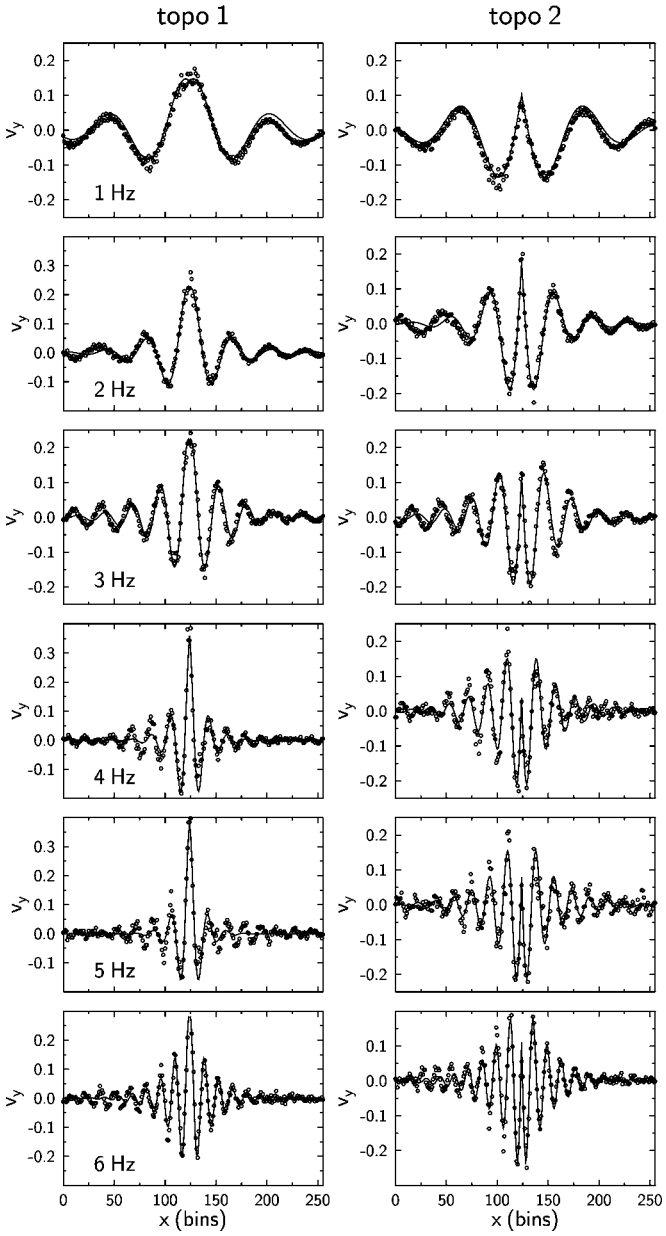

FIG. 4. The leading pair of topos 1 and 2 from the SVD analysis of shear waves in the solid phase excited at frequencies $f=1-6$ Hz (symbols). The fit functions according to Eq. (4) are shown as lines. The horizontal axis gives the position in the bins (1 bin=0.086 mm). The topos are normalized to unity.

original movies at excitation frequency ω are converted to matrices $\boldsymbol{Y}(\omega)$ with 2048 rows and 256 columns.

To prepare for the SVD analysis, we first perform a bandpass filtering on the time series. This serves two purposes: it eliminates the effect of crystal rotation, which is not interesting for the purposes of studying the wave, and it suppresses broadband noise associated with the thermal motion of the particles. This filter has 0.058 Hz total width and the central component is chosen closest to ω. The filtered matrices are then analyzed by the SVD algorithm.[20]

The leading pairs of topos resulting from the SVD analysis are compiled in Fig. 4 for the frequencies $f=1-6$ Hz. Since only the sign of the product of a topo and its associated chrono is defined, all topos are conveniently displayed with a positive value in the center of the excitation region. Because the bandpass filtering uses three FFT components, the SVD analysis yields exactly six nonzero modes. The weights of the SVD modes are compiled in Table II. Nearly the same weight factors in the first pair of modes indicate a propagating wave. The small difference of the weights can be attributed to the damping of the wave, as described above. The amplitude of the leading pair of modes decreases with excitation frequency. The signal energy of the leading pair of modes is 93.5% at 1 Hz and decreases to 81.5% at 6 Hz. This high fraction of signal energy justifies using only the leading pair of SVD modes for the further analysis. Because of the bandpass filtering the chronos of the leading pair of modes are practically sinusoidal and therefore are not displayed here.

TABLE II. Weight factors in the solid phase (no laser heating) and fraction of signal energy of the first two modes.

Mode	1 Hz	2 Hz	3 Hz	4 Hz	5 Hz	6 Hz
1	144.8	104.9	95.4	67.7	57.5	62.7
2	127.2	82.9	87.2	47.0	39.0	55.7
3	31.7	28.7	30.9	23.7	15.8	27.1
4	26.4	24.2	25.5	22.5	13.5	24.4
5	23.1	15.4	13.5	18.1	12.2	12.7
6	19.1	12.6	12.3	11.4	10.0	10.2
Fraction	93.5%	90.8%	89.7%	81.8%	87.6%	81.5%

The topos 1 and 2 in Fig. 4 are approximated by a model function that describes spatially damped sinusoidal waves of the type

$$f(x) = A\,\sin(k_r|x-x_0| + \delta)\exp(-k_i|x-x_0|). \tag{4}$$

The center point x_0 of the wave excitation region is prescribed and a four-parameter least-squares fit is used to determine the amplitude A, the real part of the wave number k_r, the phase shift δ, and the damping rate k_i. Plotting the fit parameter k_r versus the independent parameter ω for the laser excitation frequency yields a dispersion relation.

The measured wave dispersion is shown in Fig. 5. The circles and crosses represent the results from topos 1 and 2. For comparison we have applied the SFACW method described above to the unfiltered data. The result of this method is shown as squares. There is close agreement with the wave numbers determined by the SVD technique described above. This shows that the SVD analysis automatically finds the proper frequency of the wave within the bandwidth of the bandpass filter. On the contrary, for the SFACW method, the frequency must be prescribed.

At last, the dispersion of the shear wave (Fig. 5) is found to agree with theory for a triangular lattice of particles interacting with a Yukawa potential.[29] There are two theoretical curves describing wave propagation along the two principal axes of a triangular lattice (0° and 90°). The experimental data are a mixture of both principal modes because of the angular averaging due to the slow crystal rotation and bearing in mind that the plasma crystal consists of domains with different orientations.

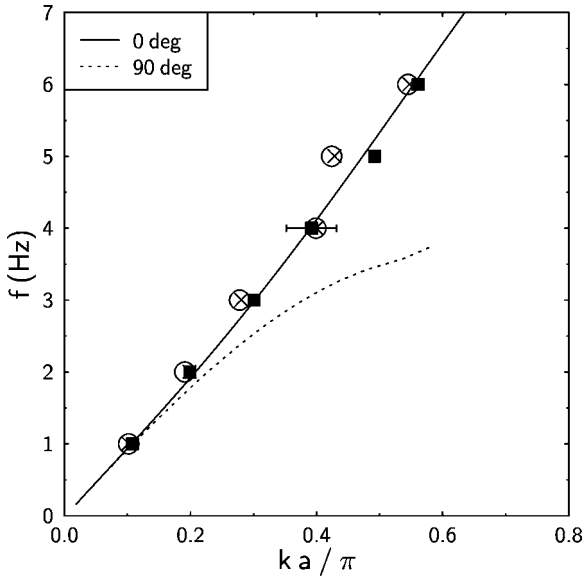

FIG. 5. Dispersion relation of shear waves in the solid phase. The measured wave numbers from topo 1 (circles) and topo 2 (crosses) are compared with the results of the SFACW method (filled squares). For comparison the dispersion curves for shear waves in a triangular lattice at propation angles 0° and 90° are shown.

VI. SHEAR WAVES IN THE LIQUID STATE

For studying shear waves at reduced values of the coupling parameter the suspension is heated by the two heating beams. At 2.3 W a liquid state with (Γ_x=128, Γ_y=158) is obtained. In performing the experiments, care is taken that the laser forces are exactly balanced and that the areas covered by the two Lissajous figures match exactly. Any small imbalance would have introduced an unwanted net flow of particles in the x direction. In order to use only the region of homogeneous dust kinetic temperature, only particle positions $102 \leqslant y \leqslant 338$ pixels are used. Since the shear waves become now strongly damped, only the central section of the image frame $200 \leqslant x \leqslant 440$ pixels is evaluated. For improving the statistics this x interval is subdivided into 64 bins and the length of the time series is 2048 frames. Again, the assignment of the particle velocities to the bins $v_y(x_j, t_i)$ is performed by interpolation with the cloud-in-cell formula.

The situation for recovering the waves in the presence of the enhanced random motion of the liquid state can be quantitatively described in terms of the power spectrum of the velocity fluctuations $P(f)$, which consists of a broad continuum on which the excited wave is superimposed with a sharp frequency peak as shown in Fig. 6(a) for the case of f_{ex}=3 Hz exciter frequency. The total kinetic energy of the wave motion, as represented by the three FFT components marked by circles, is only 2.3% of the total kinetic energy. This corresponds to a signal to noise ratio of −16.5 dB. On the other hand, the intensity of the sharp peak in the spectrum is about 10 dB above the neighboring continuum.

In a first step we have recovered the wave by the SFACW method, which uses the frequency of the highest peak in the power spectrum. The resulting spatial distribution of the Fourier amplitudes $|v_y(x)|$ are shown in Fig. 6(b) together with fit functions according to Eq. (4). This example

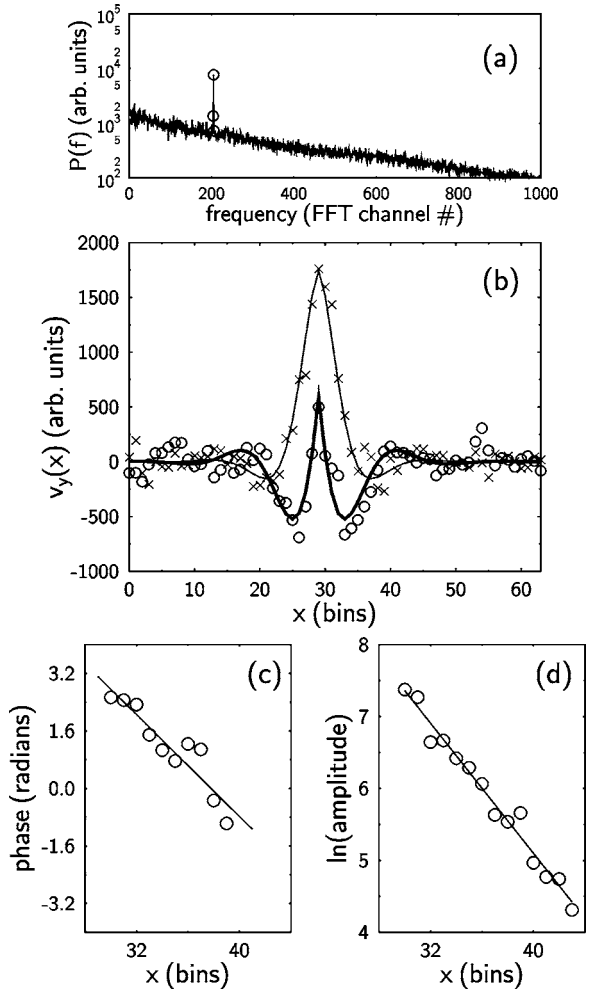

FIG. 6. (a) Power spectral density $P(f)$ of the velocity fluctuations in the observed region of wave propagation at 2.3 W heating power and 3 Hz exciter frequency. The excited shear wave has three FFT components (circles) that exceed the broadband noise. (b) Real and imaginary part of the wave functions recovered by the SFACW method and fit by Eq. (4). (c) The phase evolution of the signal propagating to the right. The slope of the fitted straight line gives k_r. (d) The logarithmic decrease of the amplitude. The slope of the fitted straight line gives k_i. The horizontal axis in (b-d) gives the position in bins (1 bin=0.13 mm).

shows that a damped wave emanates from the excited region to both sides. The wave number k_r and damping rate k_i are determined from the linear fits to the phase evolution and to the logarithmic decrement as shown in Figs. 6(c) and 6(d).

The SVD analysis follows the approach used in the case of the solid phase. Obviously, the low signal to noise ratio requires bandpass filtering of the velocity data. For this purpose, only the three components of the FFT in Fig. 6(a) that exceed the background of random fluctuations are used to provide a good signal to noise ratio. For comparison with the solid phase the first pair of topos of the SVD analysis is shown in Fig. 7 for excitation frequencies f=1–6 Hz. The measured wave signals are fitted by the function in Eq. (4). Now the shape of the topos is slightly different with respect to the oscillatory structures, which are more pronounced in topos 2 while the topos 1 show less modulation. For 1 Hz and 2 Hz, a single hump is seen in topo 2, which can be identified as representing half a wavelength of a strongly

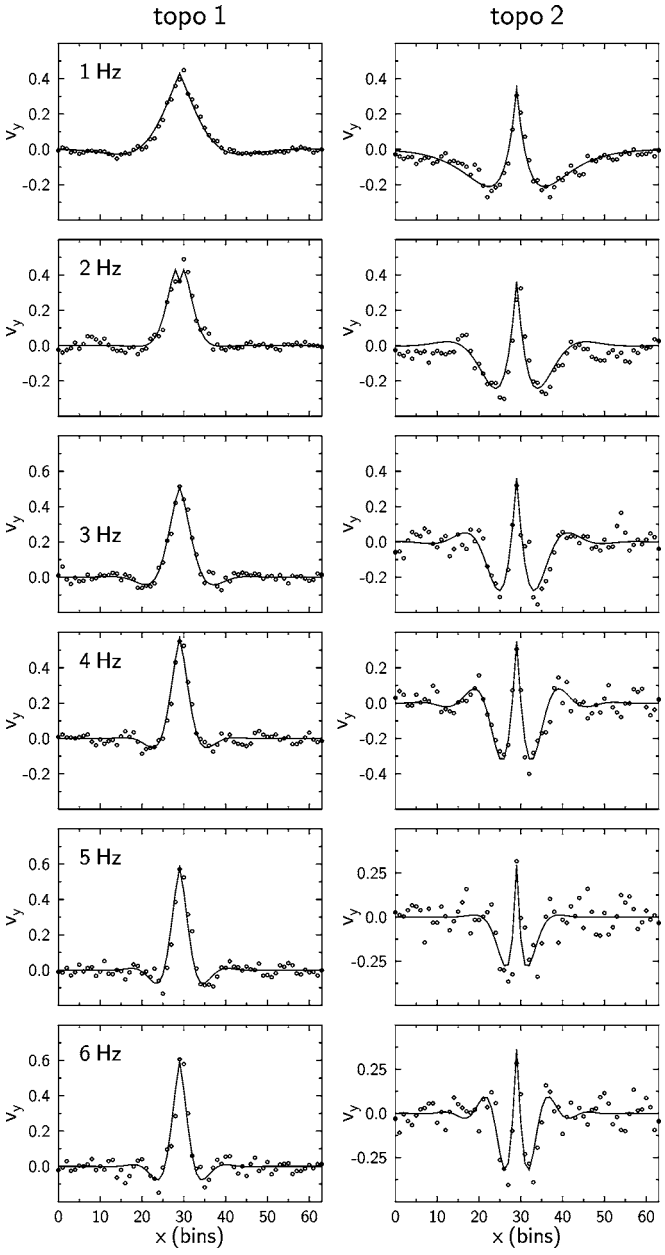

FIG. 7. The first pair of topos from the SVD analysis of shear waves in the liquid phase (2.3 W heating laser power) excited at frequencies $f=1-6$ Hz (symbols). The horizontal axis gives the position in bins (1 bin=0.13 mm). The topos are normalized to unity.

damped wave. For $f=3-6$ Hz the wavelength becomes shorter and further maxima and minima appear. The shapes of the topos 2 have a close similarity with the signals recovered by the SFACW method as shown in Fig. 6(b).

The distribution of the weight factors of the 6 SVD modes and the fraction of signal energy of the first two modes are compiled in Table III. First, we see that the wave amplitude has practically doubled according to the power increase of the excitation laser from 0.23 W to 0.46 W. Second, we find again that the signal amplitude decreases with excitation frequency. Different from the solid phase, the first two modes for excitation frequencies $f=1-6$ Hz now have unequal weights that differ by a typical factor of 2. This

TABLE III. Weight factors at 2.3 W heating laser power and fraction of signal energy of the first two modes.

Mode	1 Hz	2 Hz	3 Hz	4 Hz	5 Hz	6 Hz
1	267.8	156.7	166.4	104.4	88.9	69.8
2	138.3	75.9	60.4	50.3	41.3	34.5
3	36.4	38.1	28.1	27.9	23.1	20.6
4	32.0	33.0	25.0	23.3	22.3	16.6
5	26.7	31.4	21.9	19.4	17.7	16.1
6	23.4	29.1	20.4	17.6	14.6	13.0
Fraction	96.2%	87.4%	88.2%	87.0%	86.0%	84.3%

observation can be explained by the damping of the wave, as described in Sec. IV.

We have also tried to study the shear waves in the solid phase at conditions close to the expected melting point. For this purpose the heating laser power was set to 1.9 W, which resulted in a state with $\Gamma_x=194$, $\Gamma_y=266$ when the excitation laser was turned off. The SFACW shows that the signals have very similar shapes as those in the liquid case. The damping rate is found much stronger than in the solid when no heating is applied. The SVD analysis also shows close similarities with the shape of the topos in Fig. 7 concerning the different degree of modulation in topos 1 and 2. Again the ratio of the weights in the leading mode pair are asymmetric by the same factor as in the liquid case.

All these findings at 1.9 W heating laser power give a hint that the system was already in a liquid state. An analysis of the time averaged velocities $\bar{v}_y(x)$ shows that at 1.9 W heating laser power the maximum flow velocity in the excitation region is practically the same as in the liquid state at 2.3 W. Hence, the similarity with the liquid case can be attributed to shear induced melting by the excitation laser.

Comparison with theory

The observed wave numbers in the melting and liquid state are similar to the case of the solid phase. This is an additional hint that the observed waves are the shear waves we were searching for. In the following we compare the measured dispersion with the 2D QLCA model.[16]

The experimental points in Fig. 8(a) represent the evaluation by SFACW. For comparison the results for 1.9 W (plus with circle) and 2.3 W (crosses) are shown. The 2D QLCA model is plotted for $\kappa=0$ and $\kappa=1$, which represent a lower and an upper bound for the experimental situation with $\kappa=0.43$. Because the comparison is made in absolute quantities, the overall agreement between experiment and the 2D QLCA model is quite satisfying. Closer inspection shows that the two different values of dust temperature do not allow conclusions about a trend for the dependence on Γ.

The results from the SVD analysis are compiled in Fig. 8(b). The heating laser powers of 1.9 W (circles) and 2.3 W (squares) are compared. Open and filled symbols represent the evaluation of topos 1 and 2. The results from the SVD analysis are very similar to the SFACW method although the scatter of the data points is larger. There is a general agree-

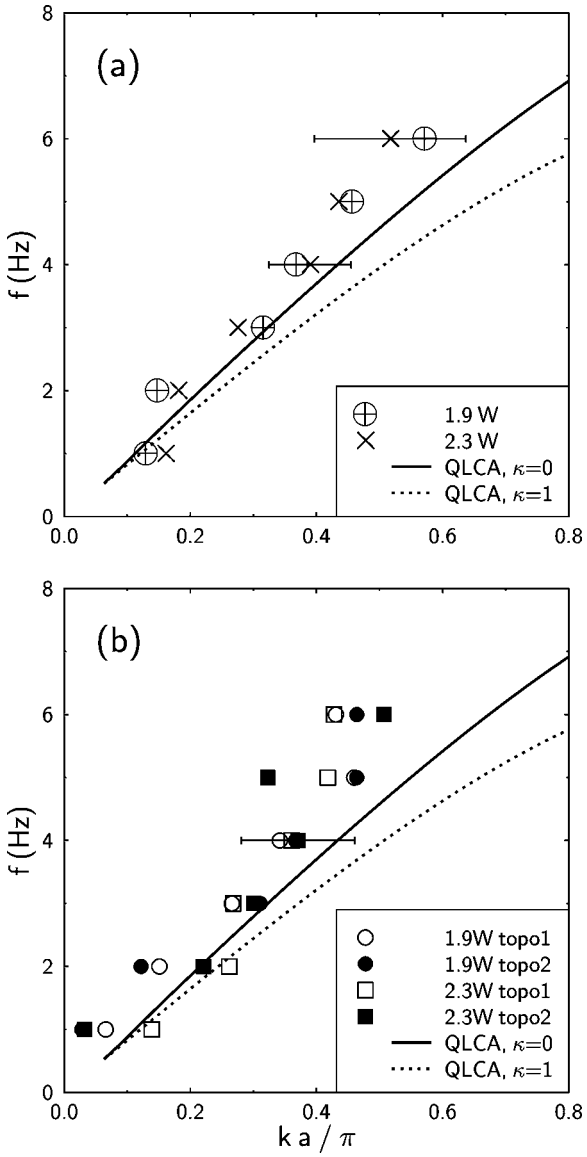

FIG. 8. (a) Comparison of the results from the SFACW method with the 2D QLCA model (Ref. 16) for two different values of κ. (b) Comparison of the SVD results with the 2D QLCA model. The symbols are defined in the insets.

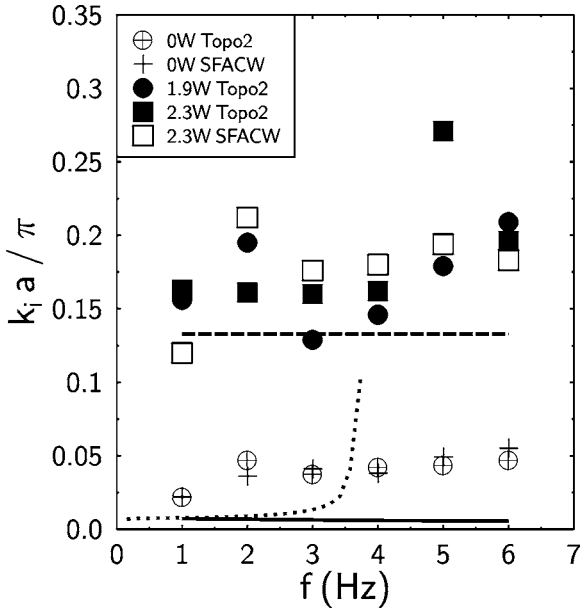

FIG. 9. Damping rate of the shear wave in the solid phase (0 W) and in the liquid phase. The results from the SFACW method and topo 2 of the SVD are compared. The expected damping of the shear wave in the solid phase by dust-neutral collisions (Ref. 29) is shown as a solid line (0°) and a dotted line (90°). An estimate of the damping rate expected for the fluid phase, as explained in the text, is shown as a dashed line. The symbols are defined in the inset.

ment with the QLCA model but the same tendency of deviation towards smaller wave numbers is found for the highest frequencies as observed above in the SFACW method.

The error bar for the wave number was estimated as follows. For the SFACW method, the error bar comprises the uncertainty of the slope of the best fit by a straight line in Fig. 6(c) as well as the influence of the choice of frequency used for the projection on Fourier modes. The latter was varied within a range of ±1% about the most probable value. The two sources of error have the same magnitude.

For the nonlinear fits by Eq. (4), first the optimum fit was determined, which yielded the most probable value for $k_{r,\mathrm{opt}}$. In a second step, the fit was repeated for given values of k_r in the range $0.5k_{r,\mathrm{opt}} < k_r < 2k_{r,\mathrm{opt}}$. The other parameters ($A$, δ, k_i) were left as free fit parameters. For each of these fits the correlation coefficient was calculated. The error bar was estimated from the point where the correlation has dropped to 90% of its maximum value. This was the same degree of decorrelation as found when the slope m of the straight line in the SFACW method was set to $m \pm \sigma_m$.

VII. DAMPING OF THE WAVES

In this section we compare the observed damping rates of the shear waves with theoretical expectations (Fig. 9). In the solid phase the damping is caused by dust neutral collisions, which were incorporated in the dispersion relation for the elastic response of a triangular lattice with a binary Yukawa potential.[29] The observed damping for propagation in the 0° direction (crosses), however, is stronger than the theoretical prediction (full line). This feature was checked by comparing the SVD result with the SFACW method, which gave identical damping constants. Hence, the disagreement with the theoretical damping is not a flaw of the SVD analysis. Higher damping rates are found in theory for the 90° direction (dotted line), which strongly increases when the group velocity becomes small for frequencies of about 3.5 Hz (see Fig. 5). Part of the difference between experiment and theory might be explained by the fact that the crystal rotation leads to a time average over different orientation angles. However, the fact that the wave numbers in Fig. 5 coincide with the 0° dispersion does not suggest an influence from the enhanced damping of the 90° direction.

For the liquid state and close to the melting point, the damping is significantly increased above its value in the solid phase. The results of the Fourier method and the SVD analysis give very similar results for the damping. Again, there is no clear trend that distinguishes the results at 1.9 W and 2.3 W.

We can make a rough estimate of the damping rate that is expected for the fluid phase as follows. For the case of weak damping, $k_i \approx \mathrm{Im}(\omega)/v_{\mathrm{ph}}$, where v_{ph} is the phase velocity for the real part of the dispersion relation. We conjecture that for a 2D liquid $\mathrm{Im}(\omega) \approx 1/(2\tau_R)$ as was reported previously for a 3D liquid,[11,14] where τ_r is a relaxation time associated with the viscoelastic response of the liquid. We further conjecture that τ_R for a 2D liquid can be estimated using the 3D theoretical result $\tau_R = [0.13\omega_{\mathrm{pd}}^{(3D)}]^{-1}$ (Refs. 11 and 14) by simply replacing $\omega_{\mathrm{pd}}^{(3D)}$ with the 2D plasma frequency $\omega_{\mathrm{pd}}^{(2D)}$ for our suspension. In this way, we obtain an estimate $k_i a/\pi = 0.13$ for our experiment, which is shown as a dashed line in Fig. 9. A more reliable theoretical estimate could be made based on a generalized hydrodynamic (GH) model for a two-dimensional Yukawa liquid, but such a theory is lacking in the literature.

VIII. SUMMARY AND CONCLUSIONS

We have demonstrated that shear waves in the liquid state of a two-dimensional particle suspension in a plasma can be excited with laser forcing. The dispersion and damping of these waves are compared with the solid phase, where the shear wave is weakly damped and can be observed with a high signal to noise ratio. In the liquid phase, the signal to noise ratio is much lower because of the higher random motion of the particles. We find a spatially oscillatory wave pattern for exciter frequencies $f = 3-6$ Hz. These waves are moderately damped with $k_i \leqslant k_r$. For smaller frequencies ($f = 1$ Hz and $f = 2$ Hz), corresponding to longer wavelengths, the wave is found to be strongly damped ($k_i > k_r$).

The SVD analysis of particle velocities turns out to be a reliable tool for extracting wave phenomena in the solid phase of the particle suspension. Propagating waves in the solid phase can be identified as a pair of topos with similar weights, which make up 81.5%–93.5% of the signal energy and can thus be considered as representative for the wave. The dispersion derived from SVD analysis is in close agreement with the SFACW technique. The difference of the two methods is the prescribed wave frequency in the SFACW technique whereas the SVD automatically selects the most probable wave frequency within the width of the bandpass filter.

The performance of the SVD method for the strongly damped waves in the liquid phase was compared with the SFACW method. We find that SVD that uses all three FFT components that exceed the neighboring continuum limit gives similar results for the wave number and damping rate as the SFACW method, but results in a larger scatter of the data.

The behavior of the shear wave close to the melting point and in the liquid phase is quite similar in dispersion and in the response amplitudes. This unexpected result can be explained by the observation that at 1.9 W heating laser power the excitation laser is sufficiently strong to break bonds and to establish a mean flow. Unfortunately, this effect was not visible on the video monitor during the experiments but only turned out in the data analysis. Hence, the waves observed at 1.9 W heating power also propagate in a local liquid state, which arises from shear-induced melting.

The comparison with the 2D QLCA model[16] is made with absolute wave numbers and gives an overall agreement with the predicted dispersion. This confirms that the excited waves are really the expected shear modes in a liquid. The estimated error bar at 3 Hz includes the $\kappa = 0$ curve. The error bars, however, increase with frequency because of the reduced signal to noise ratio.

The observed damping of the shear wave in the liquid phase is much larger than the damping of shear waves in the solid phase. An estimate based on the relaxation time for the viscoelastic response of the liquid supports this observed trend.

In summary, we have presented a first comprehensive comparison of theory and experiment for laser-excited shear waves in the solid and liquid phase of single-layer particle suspensions.

ACKNOWLEDGMENTS

The hospitality experienced at The University of Iowa is gratefully acknowledged. The authors thank P. Hartmann and G. J. Kalman for providing tabulated data of the 2D QLCA model.

The work at Iowa was supported by NASA and DOE. A. P. thanks the DFG for financial support under Grants Nos. Pi185/25-1 and SFB TR24-A2.

[1] A. Piel and A. Melzer, Plasma Phys. Controlled Fusion **44**, R1 (2002).
[2] F. M. Peeters and X. Wu, Phys. Rev. A **35**, 3109 (1987).
[3] A. Homann, A. Melzer, S. Peters, R. Madani, and A. Piel, Phys. Rev. E **56**, 7138 (1997).
[4] D. H. E. Dubin, Phys. Plasmas **7**, 3895 (2000).
[5] S. Nunomura, D. Samsonov, and J. Goree, Phys. Rev. Lett. **84**, 5141 (2000).
[6] Y. Liu, B. Liu, Y. Chen, S.-Z. Chen, L. Wang, and X. Wang, Phys. Rev. E **67**, 066408 (2003).
[7] D. Samsonov, J. Goree, Z. Ma, A. Bhattacharjee, H. M. Thomas, and G. E. Morfill, Phys. Rev. Lett. **83**, 3649 (1999).
[8] A. Melzer, S. Nunomura, D. Samsonov, and J. Goree, Phys. Rev. E **62**, 4162 (2000).
[9] V. Nosenko, J. Goree, Z. W. Ma, and A. Piel, Phys. Rev. Lett. **88**, 135001 (2002).
[10] A. Piel, V. Nosenko, and J. Goree, Phys. Rev. Lett. **89**, 085004 (2002).
[11] P. Kaw and A. Sen, Phys. Plasmas **5**, 3552 (1998).
[12] P. K. Kaw, Phys. Plasmas **8**, 1870 (2001).
[13] G. Kalman, M. Rosenberg, and H. E. DeWitt, Phys. Rev. Lett. **84**, 6030 (2000).
[14] H. Ohta and S. Hamaguchi, Phys. Rev. Lett. **84**, 6026 (2000).
[15] M. S. Murillo, Phys. Rev. E **62**, 4115 (2000).
[16] G. J. Kalman, P. Hartmann, Z. Donko, and M. Rosenberg, Phys. Rev. Lett. **92**, 065001 (2004).
[17] S. Nunomura, S. Zhdanov, D. Samsonov, and G. Morfill, Phys. Rev. Lett. **94**, 045001 (2005).
[18] J. Pramanik, G. Prasad, A. Sen, and P. K. Kaw, Phys. Rev. Lett. **88**, 175001 (2002).
[19] V. Nosenko, J. Goree, and A. Piel, Phys. Plasmas **13**, 032106 (2006).
[20] W. H. Press, S. A. Teukolsky, W. T. Vetterling, and B. P. Flannery, *Numerical Recipes in C* (Cambridge University Press, Cambridge, 1988).
[21] T. Dudok de Wit, A. L. Pecquet, J. C. Vallet, and R. Lima, Phys. Plasmas **1**, 3288 (1994).
[22] T. Dudok de Wit, Plasma Phys. Controlled Fusion **37**, 117 (1995).
[23] C. Fenzi, R. J. Fonck, M. Jakubowski, and G. R. McKee, Rev. Sci. Instrum. **72**, 988 (2001).

[24]L. Dong, Q. Zhang, and L. Wang, Rev. Sci. Instrum. **74**, 5093 (2003).
[25]P. D. Mininni, D. O. Gomez, and G. B. Mindlin, Phys. Rev. Lett. **89**, 061101 (2002).
[26]Y. Ivanov and A. Melzer, Phys. Plasmas **12**, 072110 (2005).
[27]N. Aubry and R. Lima, J. Stat. Phys. **81**, 793 (1995).
[28]R. W. Hockney and J. W. Eastwood, *Computer Simulation Using Particles* (Adam Hilger, Bristol, 1988).
[29]X. Wang, A. Bhattacharjee, and S. Hu, Phys. Rev. Lett. **86**, 2569 (2001).